Supporting information

Ruigan Hu ‡ [a], Mengyuan Zhao ‡ [b], He Miao [a,*], Fuyue Liu [a], Jiaqun Zou [a], Chunfei Zhang [a], Qin Wang [c], Ziqi Tian [b], Qiuju Zhang [b,*], Jinliang Yuan [a]

[a] Faculty of Maritime and Transportation, Ningbo University, Ningbo, 315211, PR China

[b] Ningbo Institute of Materials Technology and Engineering, Chinese Academy of Sciences, Ningbo, 315211, PR China

[c] Department of Microelectronic Science and Engineering, Faculty of Science, Ningbo University, Ningbo 315211, PR China

*Corresponding authors:

Prof. He Miao, E-mail: miaohe@nbu.edu.cn

Prof. Qiuju Zhang, E-mail: zhangqj@nimte.ac.cn

‡ These authors contributed equally to this work

■ Synthesis of perovskites

$SrNb_{0.1}Co_{0.7}Fe_{0.2}O_{3-\delta}$ (SNCF) sample was synthesized using a typical sol-gel method. First, all metal ion precursors of $Fe(NO_3)_3 \cdot 9H_2O$, $Co(NO_3)_2 \cdot 6H_2O$, $Sr(NO_3)_2$, and $C_{10}H_5NbO_{20}$ were dissolved into deionized water with stoichiometric ratio of SNCF. EDTA and citric acid were used as chelating agents, and the molar ratio of total metal ions: EDTA: citric acid = 1: 0.5: 2. Then, the solution was heated in a water bath at 80°C and stirred vigorously until the gel was completed. Then, the gel was dried at 180°C for 12 h. Finally, the prepared powder was obtained by calcination of the gel at 1200°C for 10 h. The powder was further ball milled in a planetary mill at 200 rpm for 1h using ethanol as a solvent. The other Co-based perovskites used in this study, namely $SrCo_{0.5}Fe_{0.5}O_{3-\delta}$ (SCF), $Ba_{0.5}Sr_{0.5}Co_{0.8}Fe_{0.2}O_{3-\delta}$ (BSCF), $La_{0.6}Sr_{0.4}Co_{0.8}Fe_{0.2}O_{3-\delta}$ (LSCF) were prepared by the similar sol-gel method. The SCF, BSCF and LSCF are calcined at 1000, 900 and 700 °C, respectively, for 5 h followed by ball milling at 200 rpm for 1 h.

■ Computational Details

All the geometry optimization and free energies were calculated by using Vienna ab-initio Simulation Package (VASP) [1] within Density Functional Theory (DFT) framework. The generalized gradient approximation proposed by Perdew–Burke–Ernzerh (GGA-PBE) was applied to describe the exchange–correlation functional [2, 3], while the Projector Augmented Wave (PAW) potential was used to describe the core electron interaction [4]. The cut-off kinetic energies for the plane waves were set to 500 eV [1], and the convergence criteria of energy and force on each atom after relaxation were less than 10^{-4} eV and 0.02 eV/A˚, respectively. The Brillouin zone was sampled by Gamma point [5] and a vacuum distance of 10 Å along z direction was set to ensure sufficient vaccum on surface. The Gibbs free energy (ΔG) was determined by the following equation ($\Delta G = \Delta E + \Delta E_{ZPE} - T\Delta S$), according to the normal hydrogen electrode (NHE) model proposed by Nørskov et al [6], where ΔE, ΔE_{ZPE} and ΔS correspond to the total energy change, zero point energy corrections and change of entropy, respectively. T is set to 298.15 K.

Herein, the perovskite $Sr_{20}Nb_2Co_{14}Fe_4O_{52}$ (SNCF) (001) 2 × 2 supercell with

fixing two bottom layers was built to match the experimentally-measured $SrNb_{0.1}Co_{0.7}Fe_{0.2}O_3$ quantity (Sr: Nb: Co: Fe = 10: 1: 7: 2). The removal of O and Sr at different layers was used to find out the stable vacant structures, including removing Sr and O from the surface, second and third layer. The Gibbs free energy variation (ΔG) along OER path was calculated by the following equations (1) to (4) [7].

$$\Delta G_1=\Delta G_{O*}-\Delta G_{OH*}-eU+\Delta G_{H+}\ (pH) \quad (1)$$

$$\Delta G_2=\Delta G_{OOH*}-\Delta G_{O*}-eU+\Delta G_{H+}\ (pH) \quad (2)$$

$$\Delta G_3=\Delta G_{OO*}-\Delta G_{OOH*}-eU+\Delta G_{H+}\ (pH) \quad (3)$$

$$\Delta G_4=4.92\ eV+\Delta G_{OH*}-\Delta G_{OO*}-eU+\Delta G_{H+}\ (pH) \quad (4)$$

where U was the potential determined against by NHE model at standard condition (T = 298.15 K, P = 1 bar, pH = 0) [8]. ΔG of the protons relative to the above-specified electrode at non-zero pH was represented by Nernst equation as $\Delta G_{H+}\ (pH) = -k_B T\ \ln(10) \times pH$. The overpotential (η) was defined as the lowest potential relative the NHE (1.23 V) [9, 10].

■ Faraday efficiency measurement

The gas volume (V_{mea}, mL) of oxygen evolution and hydrogen evolution is measured with a graduated cylinder. Then, the corresponding calculation is performed according to the Faraday efficiency (FE) formula:

$$Faraday\ Efficiency = \frac{m \times n \times F}{I \times t} \quad (5)$$

Where m is the actual number of moles of the product, n is the number of reaction electrons (n = 4 for OER, n = 2 for HER), F is the Faraday constant (F=96485.3383 ± 0.0083 C mol^{-1}), I is current, t is time and the subscript notation $_{mea}$ is 'measured'. The theoretical oxygen evolution and hydrogen evolution Faradaic efficiency is 100 %. The mole and actual FE conversions of the generated gas is based

on:

$$m_{mea} = \frac{V_{mea}}{V_{m}'}(mmol) \tag{6}$$

$$V_{m}' = 22.4655\ L\ mol^{-1}\ (under\ normal\ temperature\ and\ pressure)$$

(7)

$$FE = \frac{m_{mea}}{m} \times 100\ \% \tag{8}$$

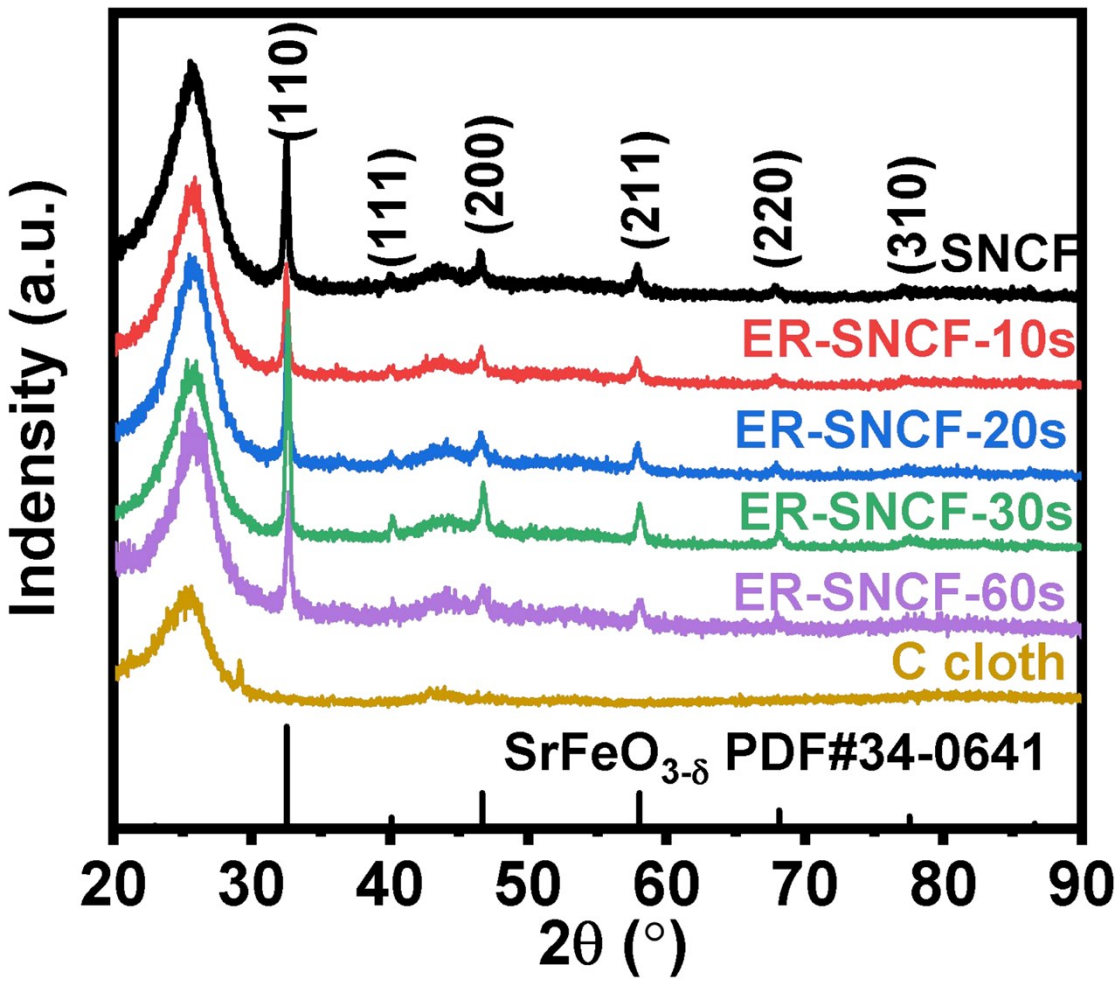

Figure S1. XRD patterns of carbon cloth, SNCF and ER-SNCF after the different electrochemical reduction times.

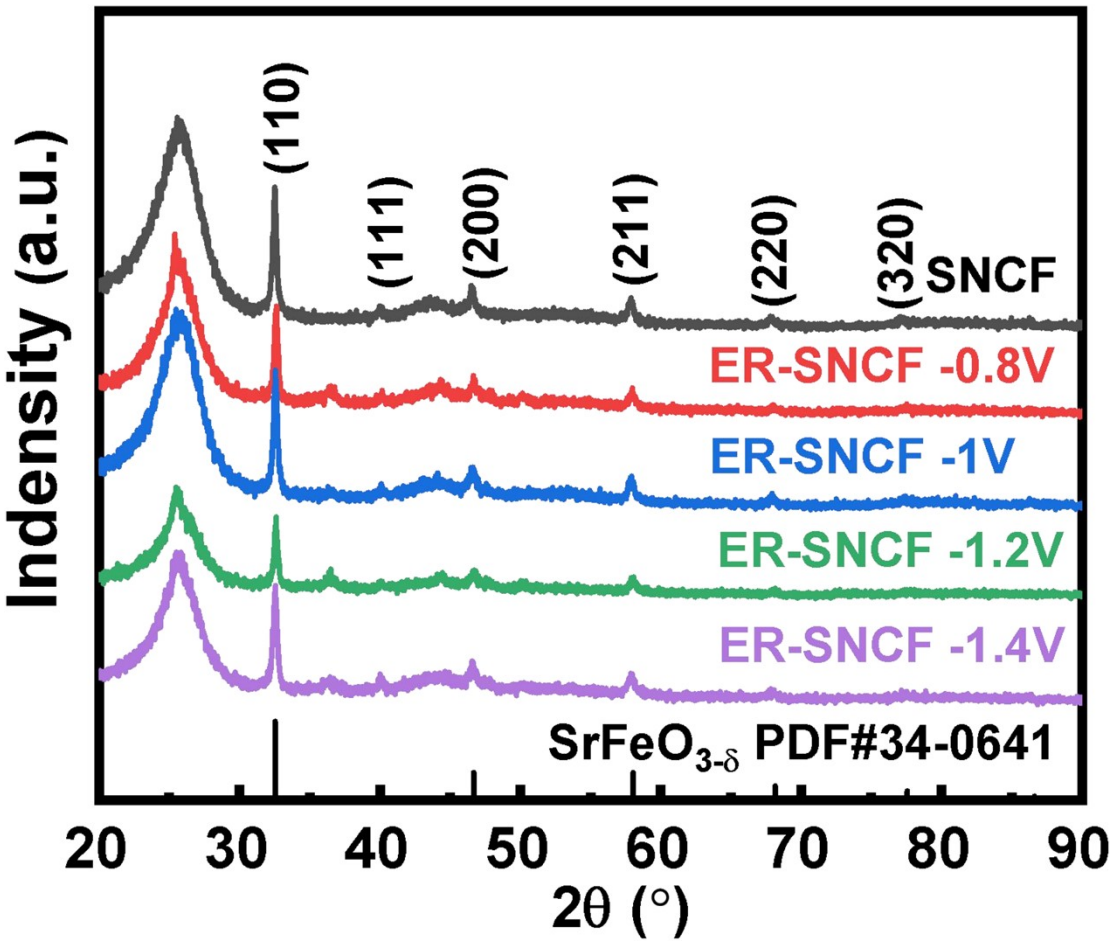

Figure S2. XRD patterns of SNCF and ER-SNCF at the different electrochemical reduction voltages.

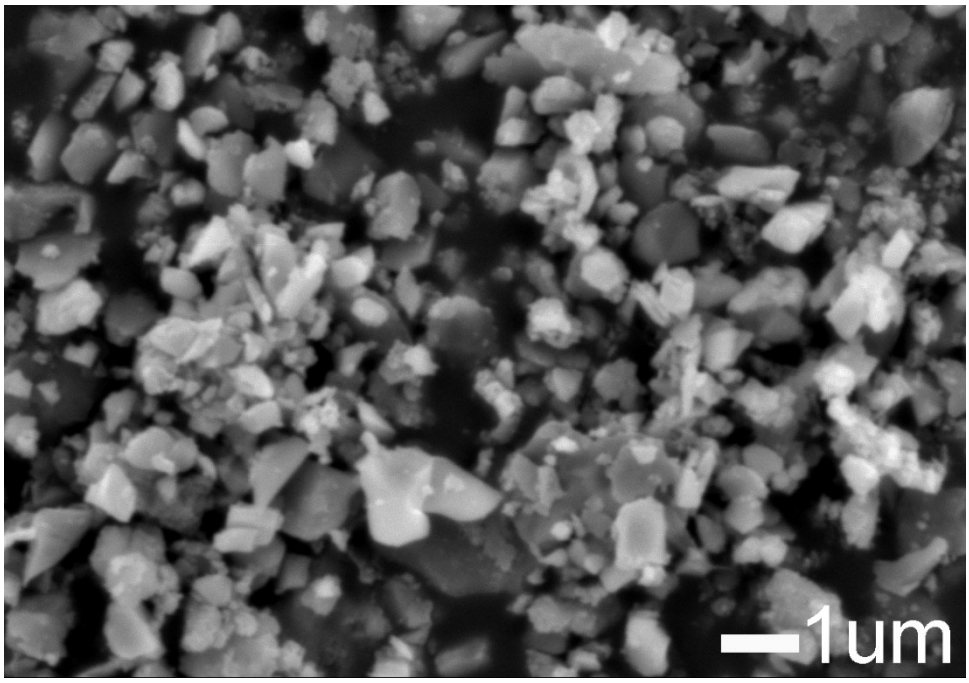

Figure S3. SEM images of SNCF.

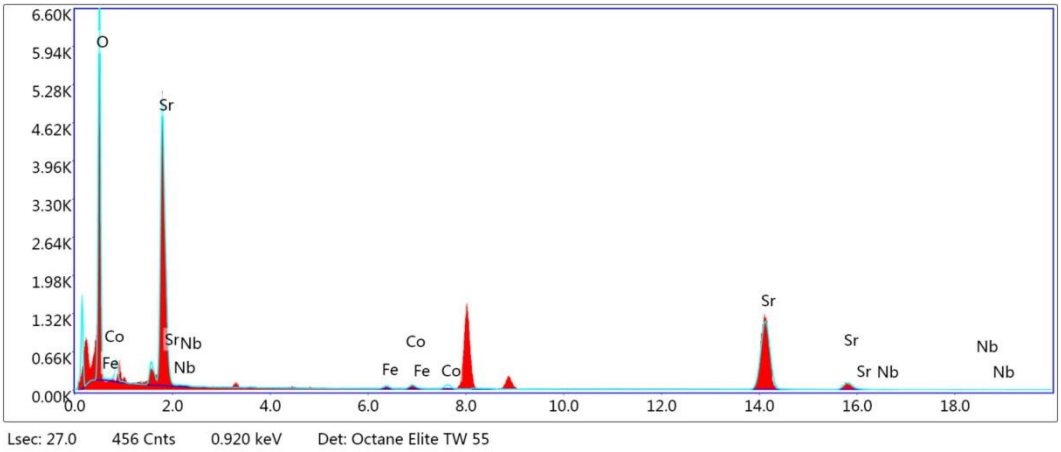

Figure S4. EDS results of nano-needles on the surface of the ER-SNCF-20s.

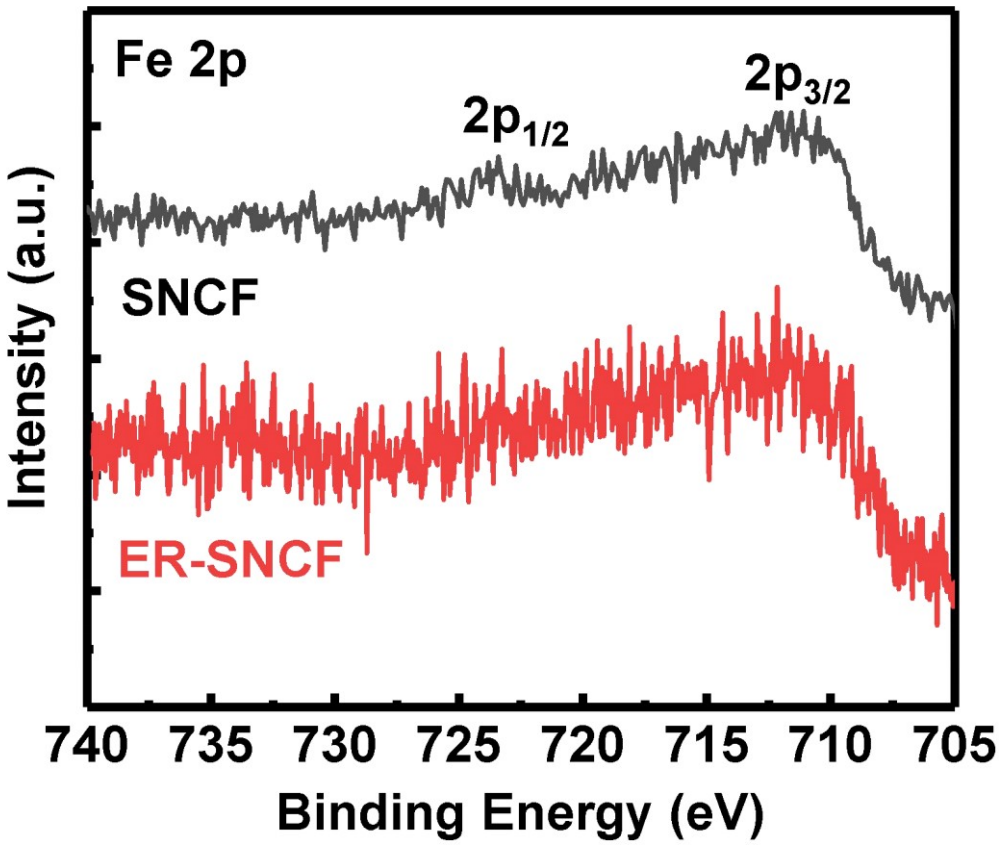

Figure S5. Fe 2p XPS spectra of SNCF and ER-SNCF.

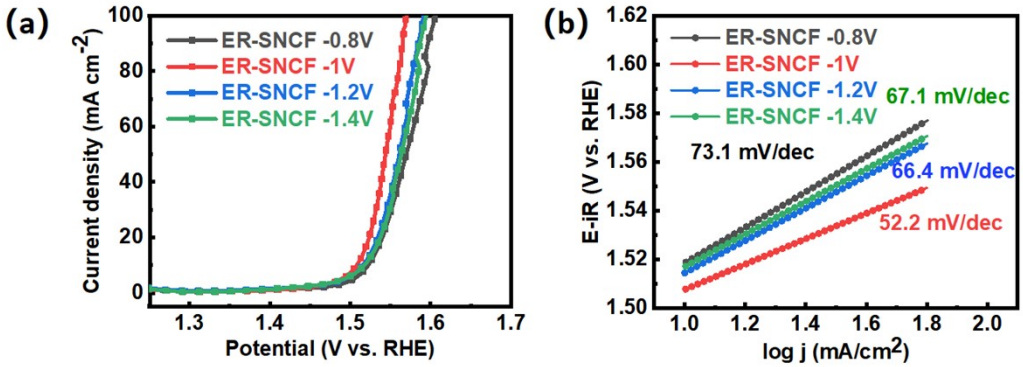

Figure S6. (a) LSV curves and (b) Tafel curves of SNCF after electrochemical reduction treatments at the different voltages.

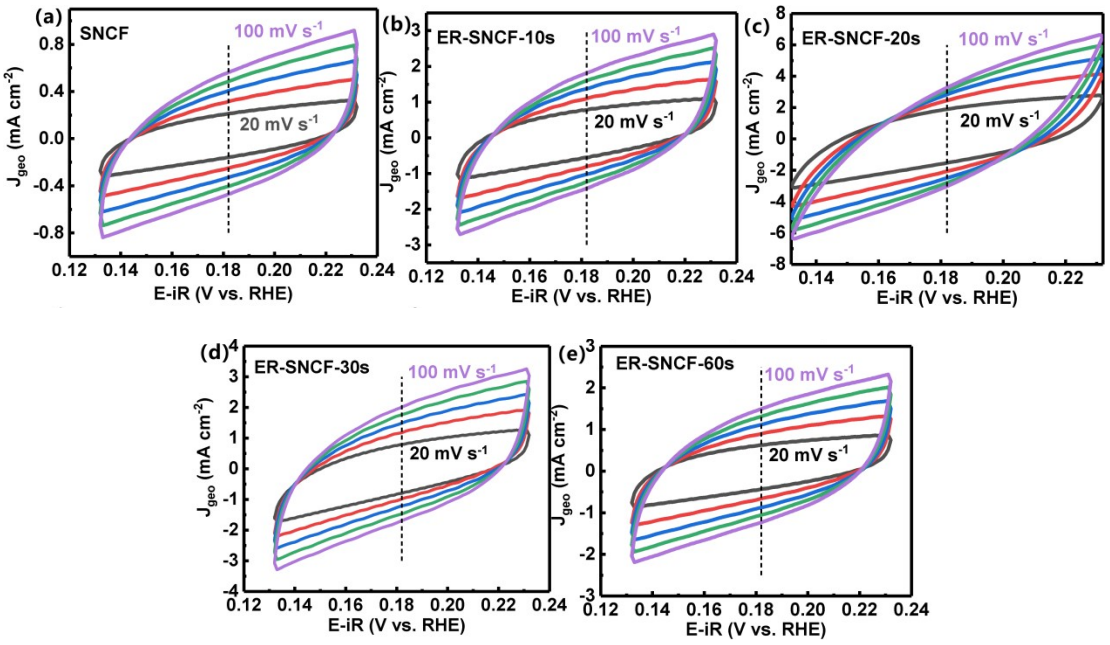

Figure S7. CV measurements in a non-faradic current region (0.132-0.232 V vs. Ag/AgCl (3.5 M KCl)) at scan rates of 20, 40, 60, 80, 100 mV s^{-1} of SNCF (a), ER-SNCF-10s (b), ER-SNCF-20s (c), ER-SNCF-30s (d) and ER-SNCF-60s (e).

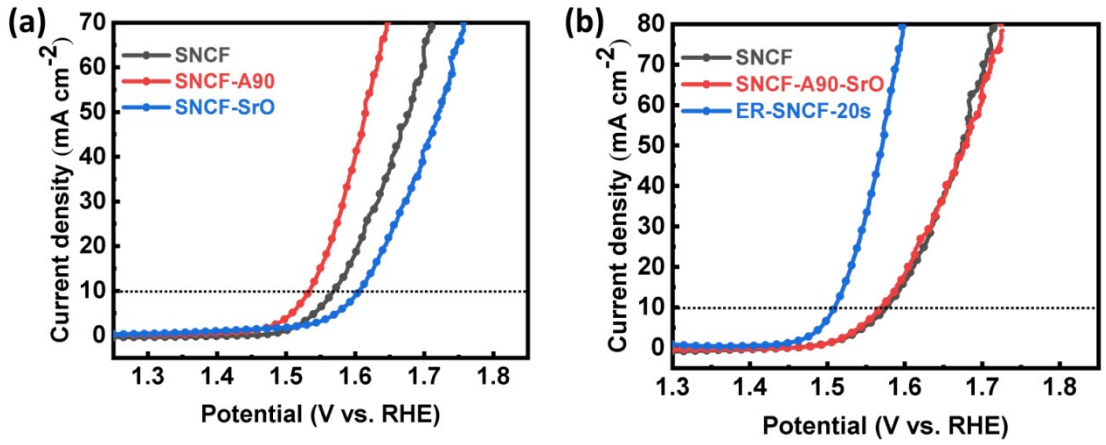

Figure S8. (a) OER LSV curves of SNCF, SNCF-A90 and SNCF-SrO. (b) OER LSV curves of SNCF, SNCF-A90-SrO and ER-SNCF-20s.

It has been reported that the SNCF with A-site cation deficiency can simultaneously introduce Sr and O vacancies[11]. Therefore, we prepare $Sr_{0.9}Nb_{0.1}Co_{0.7}Fe_{0.2}O_{3-\delta}$ (SNCF-A90) which can be utilized to represent the coexistence of Sr and O vacancies. The sample after homogeneous ball milling of SNCF with 5wt% SrO is used to represent the sample with SrO blocking. The Sr/O vacancy effects and SrO blocking effects can be investigated by comparing their OER properties with the pristine SNCF. In the Fig. S8, compared with SNCF, SNCF-A90 shows a much higher OER activity, while SNCF-SrO demonstrates a lower OER activity. This indicates that Sr/O vacancies in SNCF improve the OER activity, while SrO on the surface of SNCF deteriorates the OER activity.

We also prepared the sample of SNCF-A90-SrO by ball milling of SNCF-A90 with SrO to integrate the two effects of Sr/O vacancies and SrO block. As can be seen from Fig. S8, the OER activity of SNCF-A90-SrO is almost same with that of SNCF. Comparing with the OER activities of ER-SNCF-20s and SNCF-A90-SrO, it can be clearly seen that ER-SNCF-20s has much higher OER activity. This is due to Sr/O vacancies induced by the electrochemical reduction mainly distribute on the surface of SNCF, which reconstructs the active surface of the cobalt-based perovskite for OER [12].

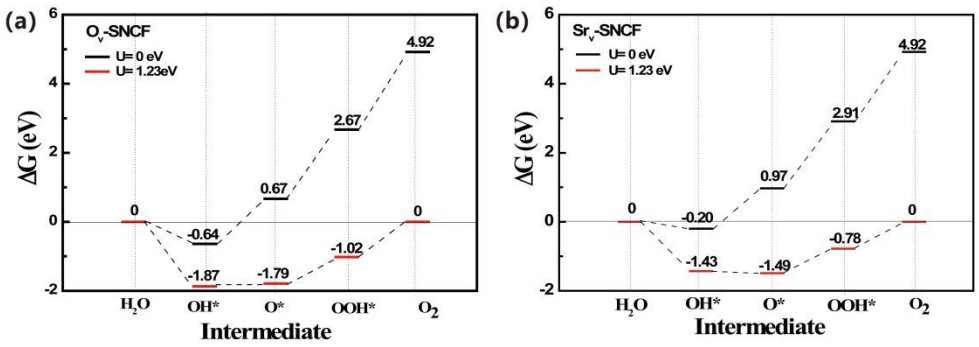

Figure S9. The Gibbs free energies (ΔG) diagram of OER evolution on surface Co site for stoichiometric O_V-SNCF and Sr_V-SNCF, respectively.

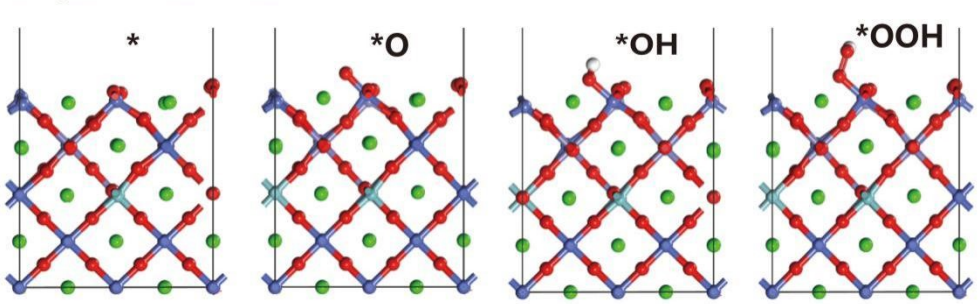

Figure S10. The geometries of intermediates for OER on Sr_VO_V-SNCF(001).

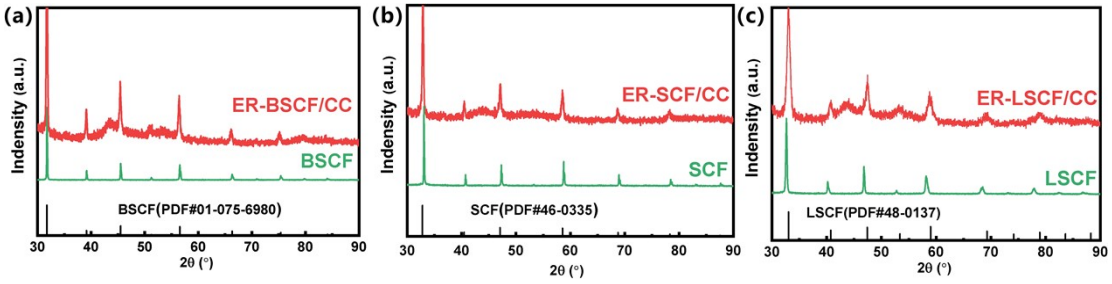

Figure S11. (a) XRD patterns of BSCF and ER-BSCF. (b) XRD patterns of SCF and ER-SCF. (c) XRD patterns of LSCF and ER-LSCF.

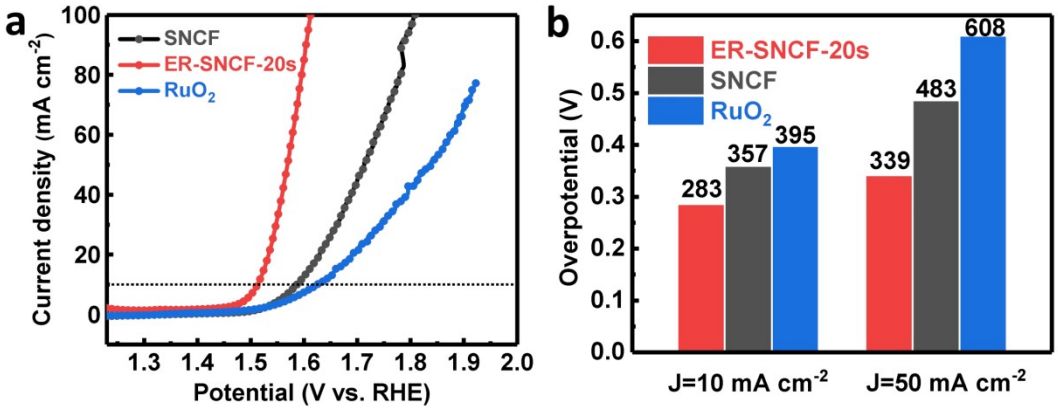

Figure S12. (a) OER LSV curves of SNCF, ER-SNCF-20s and RuO_2 in alkaline seawater. (b) Overpotentials of SNCF and ER-SNCF-20s at 10 mA cm^{-2} and 50 mA cm^{-2}.

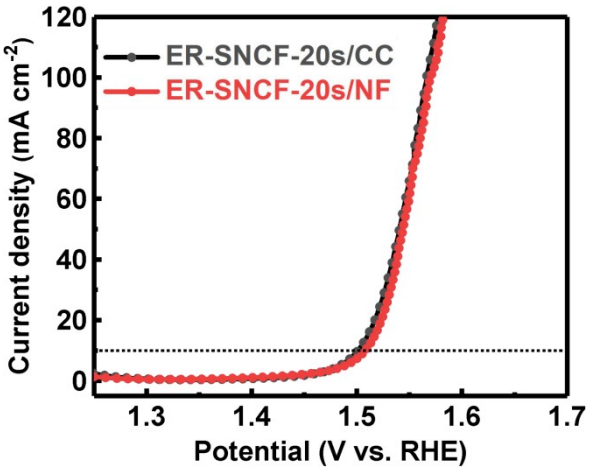

Figure S13. OER LSV curves of ER-SNCF-20s with different substrates of nickel foam (NF) and carbon cloth (CC).

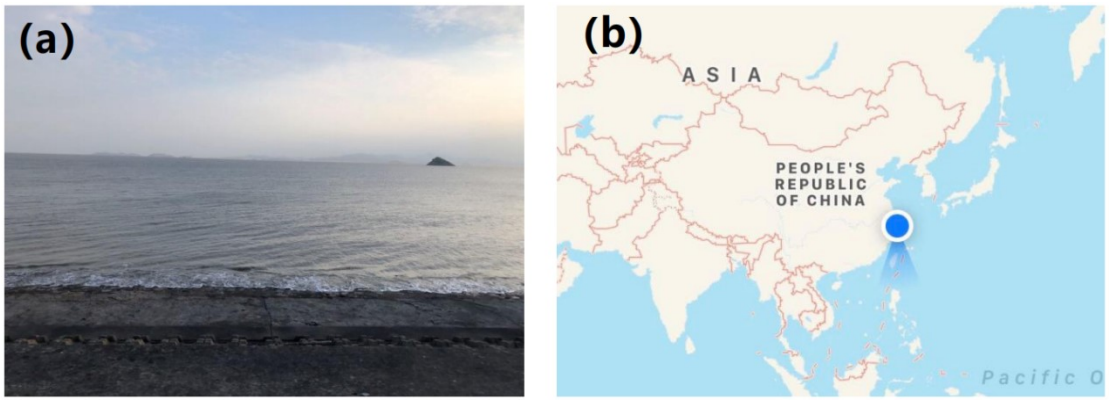

Figure S14. (a) Seawater collection location in this work. (b) Seawater was collected from the East China Sea (29°52'00.00"N, 121°31'00.00"E).

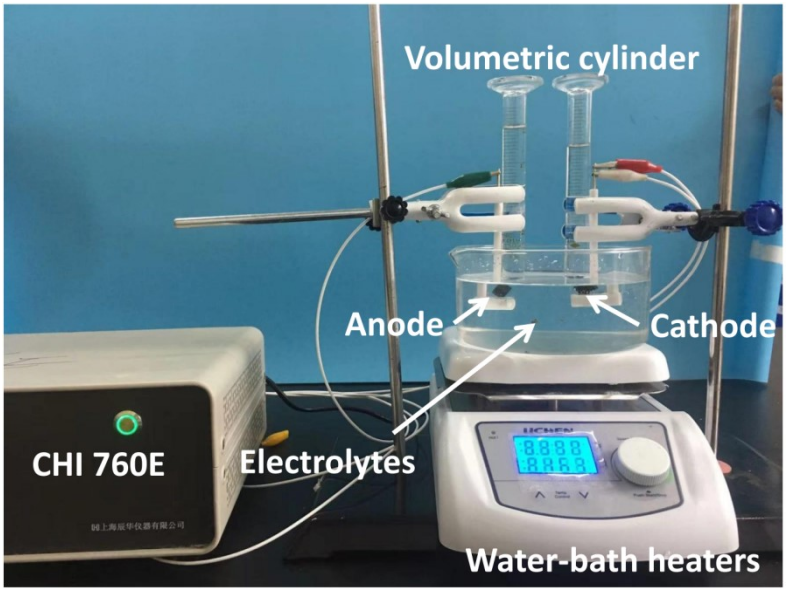

Figure S15. Diagram of the Faraday efficiency test device.

Table S1. XPS quantitative analyses (atomic percentages) of Co 2p and O 1s in SNCF and ER-SNCF-20s.

Sample	Co^{3+} ($2p_{3/2}$)	Co^{2+} ($2p_{3/2}$)	Co^{3+}/Co^{2+}	O^{2-}	O_2^{2-}/O	O_{surf}	H_2O
SNCF	33.57	11.7	2.87	8.96	15.74	60.33	14.97
ER-SNCF-20s	38.58	19.82	1.94	3.01	25.08	58.97	12.94

Table S2. Oxygen catalytic performances of SNCF, ER-SNCF, ER-BSCF, ER-LSCF, and ER-SCF.

Samples	η @ 10 mA cm^{-2} (mV)	OER Tafel slopes (mV dec^{-1})
SNCF	341	91.9
ER-SNCF-10s	302	65.7
ER-SNCF-20s	278	56
ER-SNCF-30s	314	69.8
ER-SNCF-60s	314	74.7
ER-SNCF--0.8V	293	73.1
ER-SNCF--1V	278	52.2
ER-SNCF--1.2V	286	66.4
ER-SNCF--1.4V	288	67.1
ER-BSCF	284	59.6
ER-LSCF	306	70.4
ER-SCF	265	45.2

Table S3. Comparison of OER activities of the different types of Co-based catalysts in this work and the other reports.

Sample	Electrolyte	η @ 10 mA cm^{-2} (mV)	Tafel slope (mV dec^{-1})	Reference
ER-SNCF-20s	1M KOH	278	56	This
IrO_2	1M KOH	344	/	work
BSCF	1M KOH	420	/	[13]
BSCF-NFs	1M KOH	370	/	[13]
CQD@BSCF-NFs	1M KOH	350	/	[13]
F-BSCF	1M KOH	280	101.67	[14]
SNCF-NR	1M KOH	370	48	[15]
Co_3O_4/rm-GO	1M KOH	310	67	[16]
CoMn LDH	1M KOH	324	43	[17]
CoCo LDH	1M KOH	393	59	[18]
Co9S8@MoS2/CNFs	1M KOH	430	61	[19]
CoMnP nanoparticles	1M KOH	330	95	[20]
ER-Co_3O_4 NWs-	1M KOH	344	50	[21]

References:

1. G. Kresse and J. Furthmüller, *Physical review B*, 1996, **54**, 11169.
2. J. P. Perdew, K. Burke and M. Ernzerhof, *Physical review letters*, 1996, **77**, 3865.
3. J. P. Perdew and Y. Wang, *Phys Rev B Condens Matter*, 1992, **46**, 12947-12954.
4. P. E. Blochl, *Phys Rev B Condens Matter*, 1994, **50**, 17953-17979.
5. H. J. Monkhorst and J. D. Pack, *Physical Review B*, 1976, **13**, 5188-5192.
6. A. A. Peterson, F. Abild-Pedersen, F. Studt, J. Rossmeisl and J. K. Nørskov, *Energy & Environmental Science*, 2010, **3**.
7. J. Rossmeisl, A. Logadottir and J. K. Nørskov, *Chemical Physics*, 2005, **319**, 178-184.
8. J. K. Nørskov, J. Rossmeisl, A. Logadottir, L. Lindqvist, J. R. Kitchin, T. Bligaard and H. Jonsson, *The Journal of Physical Chemistry B*, 2004, **108**, 17886-17892.
9. A. D. Doyle, J. H. Montoya and A. Vojvodic, *ChemCatChem*, 2015, **7**, 738-742.
10. I. C. Man, H. Y. Su, F. Calle‐Vallejo, H. A. Hansen, J. I. Martínez, N. G. Inoglu, J. Kitchin, T. F. Jaramillo, J. K. Nørskov and J. Rossmeisl, *ChemCatChem*, 2011, **3**, 1159-1165.
11. H. Liu, X. Ding, L. Wang, D. Ding, S. Zhang and G. Yuan, *Electrochimica Acta*, 2018, **259**, 1004-1010.
12. Y. Zhu, L. Zhang, B. Zhao, H. Chen, X. Liu, R. Zhao, X. Wang, J. Liu, Y. Chen and M. Liu, *Advanced Functional Materials*, 2019, **29**.
13. H. Li, L. Ma, C. Han, Z. Wang, Z. Liu, Z. Tang and C. Zhi, *Nano Energy*, 2019, **62**, 550-587.
14. J. Xiong, H. Zhong, J. Li, X. Zhang, J. Shi, W. Cai, K. Qu, C. Zhu, Z. Yang, S. P. Beckman and H. Cheng, *Applied Catalysis B: Environmental*, 2019, **256**.
15. Y. Zhu, W. Zhou, Y. Zhong, Y. Bu, X. Chen, Q. Zhong, M. Liu and Z. Shao, *Advanced Energy Materials*, 2017, **7**.
16. Y. Liang, Y. Li, H. Wang, J. Zhou, J. Wang, T. Regier and H. Dai, *Nat Mater*, 2011, **10**, 780-786.
17. F. Song and X. Hu, *J Am Chem Soc*, 2014, **136**, 16481-16484.
18. F. Song and X. Hu, *Nat Commun*, 2014, **5**, 4477.
19. H. Zhu, J. Zhang, R. Yanzhang, M. Du, Q. Wang, G. Gao, J. Wu, G. Wu, M. Zhang, B. Liu, J. Yao and X. Zhang, *Adv Mater*, 2015, **27**, 4752-4759.
20. D. Li, H. Baydoun, C. N. Verani and S. L. Brock, *J Am Chem Soc*, 2016, **138**, 4006-4009.
21. S. Liu, H. Cheng, K. Xu, H. Ding, J. Zhou, B. Liu, W. Chu, C. Wu and Y. Xie, *ACS Energy Letters*, 2018, **4**, 423-429.